ACS APPLIED ELECTRONIC MATERIALS

Article

Cite This: ACS Appl. Electron. Mater. XXXX, XXX, XXX−XXX

pubs.acs.org/acsaelm

Organic Bulk Heterojunction Infrared Photodiodes for Imaging Out to 1300 nm

Weichuan Yao,[†] Zhenghui Wu,[†] Eric Huang,[‡] Lifeng Huang,[§] Alexander E. London,[§] Zhaowei Liu,[†] Jason D. Azoulay,[§] and Tse Nga Ng*,[†]

[†]Department of Electrical and Computer Engineering, University of California San Diego, 9500 Gilman Drive, La Jolla, California 92093-0407, United States

[‡]Department of Physics, University of California San Diego, 9500 Gilman Drive, La Jolla, California 92093-0407, United States

[§]Center for Optoelectronic Materials and Devices, School of Polymer Science and Engineering, School of Polymer Science and Engineering, University of Southern Mississippi, 118 College Drive, No. 5050, Hattiesburg, Mississippi 39406, United States

Supporting Information

ABSTRACT: This work studies organic bulk heterojunction photodiodes with a wide spectral range capable of imaging out to 1.3 μm in the shortwave infrared. Adjustment of the donor-to-acceptor (polymer:fullerene) ratio shows how blend composition affects the density of states (DOS) which connects materials composition and optoelectronic properties and provides insight into features relevant to understanding dispersive transport and recombination in the narrow bandgap devices. Capacitance spectroscopy and transient photocurrent measurements indicate the main recombination mechanisms arise from deep traps and poor extraction from accumulated space charges. The amount of space charge is reduced with a decreasing acceptor concentration; however, this reduction is offset by an increasing trap DOS. A device with 1:3 donor-to-acceptor ratio shows the lowest density of deep traps and the highest external quantum efficiency among the different blend compositions. The organic photodiodes are used to demonstrate a single-pixel imaging system that leverages compressive sensing algorithms to enable image reconstruction.

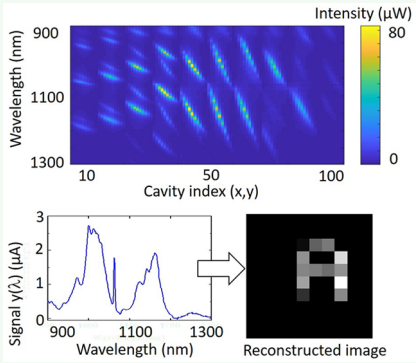

KEYWORDS: *organic photodetector, infrared, density of states, compressive sensing, capacitance spectroscopy, space charge accumulation*

INTRODUCTION

Shortwave infrared (SWIR wavelength, λ = 1−3 μm) imaging technologies are essential to many environmental monitoring and medical applications,[1] but their cost remains prohibitive for widespread application. Solution-processed organic semiconductors offer the potential to lower processing costs[2−6] and realize economical SWIR imagers. The recent progress in tuning narrow bandgap polymers[7−10] has enabled organic bulk heterojunction (BHJ) photodiodes to show a photoresponse out to 1.7 μm; however, the device external quantum efficiency (EQE) is limited, with EQE $\leq$ 30% in state-of-the-art organic SWIR photodiodes not using photoconductive gain.[11−13] The device EQE and detectivity (D^*) are low due to increasing nonradiative recombination[14,15] because the bandgap is reduced. To understand the recombination mechanisms in SWIR BHJ devices, this work examines the density of states (DOS) distribution and carrier transit time through capacitance[16,17] and transient photocurrent[18,19] measurements. The sub-bandgap DOS is important, because the DOS connects the materials composition and optoelectronic properties and provides an understanding of dispersive transport and recombination, particularly at localized trap states.[20]

Here we adjust the BHJ donor-to-acceptor ratio to study how blend composition affects the DOS and in turn influences charge transport in narrow bandgap devices. Prior reports have shown that higher fullerene acceptor concentration raises polarizability and dielectric screening in BHJ and improves charge-transfer (CT) state dissociation.[21−23] This work offers insight into another aspect of the donor-to-acceptor ratio, namely, on how it affects the recombination and charge collection process. As the blend ratio is tuned, we identify two recombination mechanisms, one due to deep traps and the other to poor extraction of accumulated space charges at the electrodes. On the basis of the device characterization, the optimal composition is used to fabricate a device for imaging in the spectral range of 1−1.3 μm. We incorporate an etalon array with a single photodiode and, through a compressive sensing algorithm,[24−26] reconstruct the captured image, demonstrating the potential of using these solution-processed organic devices for SWIR imaging applications.

Received: January 4, 2019
Accepted: April 15, 2019
Published: April 15, 2019

Downloaded via UNIV OF CALIFORNIA SAN DIEGO on May 8, 2019 at 23:35:41 (UTC).
See https://pubs.acs.org/sharingguidelines for options on how to legitimately share published articles.

© XXXX American Chemical Society

DOI: 10.1021/acsaelm.9b00009
ACS Appl. Electron. Mater. XXXX, XXX, XXX−XXX

Table 1. Parameters of Equation 3 That Fit the Capacitance−Frequency Curves in Figure 2a

		Gaussian distribution			exponential distribution	
D:A	thickness (nm)	N_G (10^{15} cm^{-3})	σ (meV)	E_{G0} (meV)	N_T (10^{20} cm^{-3} eV^{-1})	E_T (meV)
1:1	160	6.2 ± 0.1	69 ± 3	500 ± 2	0.96 ± 0.02	40.0 ± 0.1
1:2	190	5.7 ± 0.1	87 ± 3	505 ± 2	0.84 ± 0.02	40.0 ± 0.1
1:3	160	3.4 ± 0.1	62 ± 2	499 ± 2	3.41 ± 0.02	36.0 ± 0.1
1:4	120	3.8 ± 0.1	76 ± 4	530 ± 2	4.42 ± 0.02	37.0 ± 0.1

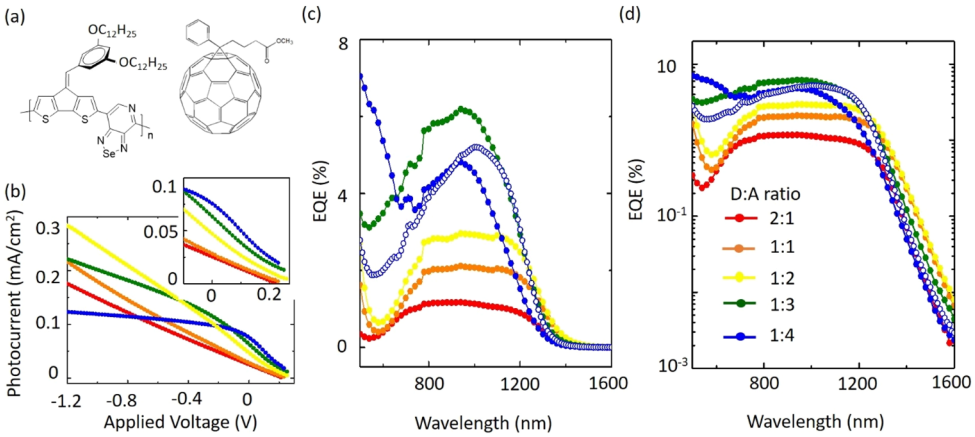

Figure 1. (a) Chemical structures of the polymer and fullerene derivative. (b) Photocurrent versus applied voltage under incident broad spectrum white light with the intensity of 4 mW/cm^2. The light intensity was kept low to ensure all of the measurements were in the linear dynamic range of the devices. The inset zooms in near the built-in bias. The various colors indicate different donor to acceptor ratios. External quantum efficiency at zero applied bias versus incident wavelength, in (c) linear scale and (d) logarithmic scale. The BHJ film thickness for each D:A ratio is 180 nm for 2:1, 160 nm for 1:1, 190 nm for 1:2, 160 nm for 1:3, and 120 nm (blue solid symbols) and 200 nm (blue open symbols) for 1:4.

■ EXPERIMENTAL METHODS

The synthesis process and basic chemical properties of the polymer C=CPhCDT-*co*-PSe are described in ref 10 and in the Supporting Information. The fullerene derivative $PC_{61}BM$ was purchased from Ossila Ltd. The chemicals were used as received without further purification. The device fabrication process is described in ref 9. In brief, poly(3,4-ethylenedioxythiophene):poly(styrenesulfonate) (PEDOT:PSS; Heraeus 4083) was diluted with isopropanol in 1:4 volume ratio to improve substrate surface wetting. The diluted PEDOT:PSS was cast onto a cleaned ITO substrate and annealed at 130 °C for 10 min to form the hole extraction interfacial layer. The solvent for the BHJ blends was a mixture of chlorobenzene and chloroform in 3:1 volume ratio, with 3% 1,8-diiodooctane as an additive. C=CPhCDT-*co*-PSe and $PC_{61}BM$, in the weight ratio ranging from 2:1 to 1:4, were dissolved into the solvent. Each solution was stirred at 55 °C overnight inside a nitrogen-filled glovebox before being spin-coated. The device thicknesses in Table 1 were measured by a Dektak 150 surface profiler. A ZnO nanoparticle solution was spin-coated onto the BHJ layer to form an ∼15 nm electron extraction interfacial layer. Then 80 nm Al was thermally evaporated to finish the photodiode structure. The devices were encapsulated with cover glass slides glued onto the substrates with epoxy.

The device characterization equipment is described in ref 9. The EQE is calculated with the expression $EQE = R(hc/\lambda q) = (J_{ph}/P_{illumin})(hc/\lambda q)$, where h is Planck's constant, c is the speed of light, λ is the wavelength of the incident light, q is the electron charge, J_{ph} is the photocurrent density, $P_{illumin}$ is the intensity of the incident light, and R is the responsivity.

For transient photocurrent measurements, the light source was a 520 nm pulsed laser with <10 ns pulse width. The RC time is measured to be ∼90 ns, which is much shorter compared to the carrier transit time. Laser intensity was 20 mW/cm^2 and kept the same for all measurements in the linear dynamic range of the devices. The photodiode was in series with a load resistor of 150 Ω, and the photocurrent was converted from the voltage dropped across the load resistor ($I = V/(150\ \Omega)$). A set of 64 measurements was averaged and recorded by an oscilloscope, and the curves in Figure 3 are the average over five trials for each applied bias.

In capacitance spectroscopy measurements, a small ac voltage of 100 mV was used and this amplitude was chosen to maintain the linearity of the response and minimize the measurement noise. The noise spectral density was measured through a preamplifier (SRS 570) connected to a power spectrum analyzer (HP 89410A).

Measurement Process for Image Reconstruction. The Fabry−Perot cavity array was fabricated using grayscale electron-beam lithography as previously described by Huang et al.[25,26] The area of each cell in the cavity array is 500 × 500 μm^2. The light source was a supercontinuum laser (NKT Photonics SuperK COMPACT), and the white light was passed through a monochromator (Horiba iHR 550) to modulate the output wavelength over time. An infrared camera (Hamamatsu C12741-03) was used to capture the transmission pattern of the cavity array for calibration. The calibration pattern was adjusted by a ratio of spectral responsivity, to account for the difference in spectral response between the infrared camera and the organic SWIR photodiode. The sample to be imaged was a mask patterned by inkjet printing black ink to block light transmission. Since the black ink did not completely block out all SWIR light, a small signal from the light leakage was subtracted from the background. The photocurrent from our organic device was collected with a lock-in amplifier (SRS 830) and a data acquisition board (NI USB-6009). The compressive sensing algorithm for image reconstruction is based on L1-regularized least-squares method, as described by Kim et al.[24]

■ RESULTS AND DISCUSSION

The photodiode semiconductors are a blend of the copolymer[10] comprised of a bridgehead olefin (C=CPh) substituted cyclopentadithiophene (CDT) donor and pyridal-[2,1,3]selenadiazole (PSe) acceptor (C=CPhCDT-*co*-PSe) and the molecule [6,6]-phenyl-C_{61}-butyric acid methyl ester ($PC_{61}BM$). The polymer has a peak absorption at λ = 950

DOI: 10.1021/acsaelm.9b00009
ACS Appl. Electron. Mater. XXXX, XXX, XXX−XXX

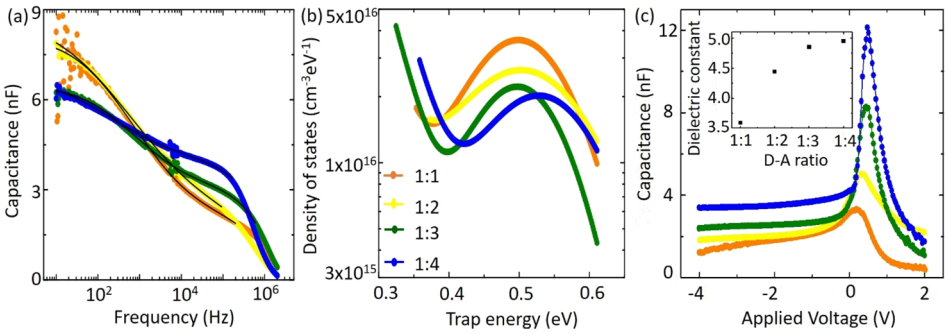

Figure 2. (a) Capacitance versus frequency at zero applied bias. The markers represent the experimental data, and the black solid lines are calculated fits using eqs 2 and 3. (b) Density of states extracted from panel a. (c) Capacitance versus applied voltage at 10 kHz. Inset: dielectric constants extracted from the capacitance measurements at a bias of −4 V. All of the measurements are taken in the dark.

nm, and the devices show the photoabsorption edge to λ = 1300 nm as shown in Figure 1. The BHJ energy band diagram of the polymeric donor and the fullerene-derivative acceptor is illustrated in Supporting Information Figure S1. The photocurrent near the built-in potential, V_{bi}, in Figure 1b shows "s-shaped" kinks which indicate non-ideal charge extraction. The V_{bi} is defined[27] as the voltage when J_{ph} = 0, where the photocurrent is the photoresponse $J_{illumin}$ subtracted by the dark current J_{dark} as shown in Supporting Information Figure S2.

As the weight ratio of donor-to-acceptor (D:A) is varied from 2:1 to 1:4, the photocurrent shows lower electric-field dependence with increasing acceptor concentration. The BHJ with 1:3 ratio reaches the highest EQE of 6.2% without an external bias in Figure 1c. If a reverse bias of −0.65 V is applied to this photodiode, the EQE increases by ∼2 times due to the electric-field dependence as seen in Figure 1b. Devices with a 1:4 ratio are made with two different film thicknesses, to check if optical absorbance (Supporting Information Figure S3) contributes to the EQE decrease beyond a 1:3 ratio. As the film thickness is increased from 120 to 200 nm, the devices with 1:4 ratio still show lower EQE than the device with 1:3 ratio. As the film thickness increases, a shift of the EQE peak for the device with 1:4 ratio is observed. This shift is caused by different distributions of the light intensity due to the optical interference effect in different film thicknesses.

Different D:A ratios are shown to affect morphologies such as crystalline packing and aggregation,[28] therefore resulting in the change of DOS. The measurements below extract the DOS to determine the electronic state distribution. Knowing the DOS will help to reveal recombination mechanisms and explain why a 1:3 ratio is the optimal composition in our set of SWIR devices.

Capacitance Measurements in the Dark. The DOS is extracted from capacitance−frequency measurements,[17,29] which determine the fraction of trap charge responding to an applied ac field that thermally excites trapped charges to mobile transport states. The small ac bias alternately traps and releases carriers from states near the Fermi energy. The trap energy is expressed as a function of the measurement frequency by

$$E_\omega = kT \ln\left(\frac{\omega_0}{\omega}\right) \tag{1}$$

where k is Boltzmann's constant, T is the temperature, and ω_0 is the rate prefactor for thermal excitation from the trap and around 10^{12} s^{-1} in typical organic photodiodes.[17] Based on analyses in refs 17 and 29, the trap DOS distribution is

$$\mathrm{DOS}(E_\omega) = -\frac{V_{bi}}{qAtkT}\frac{\mathrm{d}C(\omega)}{\mathrm{d}\ln(\omega)} \tag{2}$$

where V_{bi} is the built-in potential, q is the electric charge, and $C(\omega)$ is the capacitance measured with an ac perturbation of angular frequency, ω. Here V_{bi} ranges from 0.25 to 0.3 V for different D:A ratios, and temperature is ∼300 K. The device area is A = 9 mm^2, and the BHJ thickness, t, is listed in Table 1. Note that electron and hole traps cannot be distinguished in the capacitance measurement and their sum is reported.

A rapid change in slope $\mathrm{d}C/(\mathrm{d}\ln(\omega))$ reflects an increase of the trap DOS at the corresponding energy by eq 2. The device with a D:A ratio of 2:1 showed the worst initial performance among the series; its characteristics degraded rapidly and were omitted in the following analyses. In Figure 2a, in the high-frequency region between 0.1 and 1 MHz, the devices generally have a large DOS as evident from the rapidly changing capacitance. Then the DOS decreases in the range between 1 kHz and 0.1 MHz but rises again at a low frequency below 1 kHz. This trend indicates the presence of separated groups of shallow and deep traps located at different energy levels. To quantitatively describe this trend, we express the DOS as a combination[17,30] of an exponential distribution for the band-tail with shallow traps and a Gaussian distribution for the deep states:

$$\mathrm{DOS}(E_\omega) = N_T \exp\left(\frac{-E_\omega}{E_T}\right) + \frac{N_G}{\sigma\sqrt{2\pi}} \exp\left[-\frac{(E_\omega - E_{G0})^2}{2\sigma^2}\right] \tag{3}$$

In the first term denoting the exponential distribution, N_T is the density of states near the mobility edge and E_T is the slope of the exponential band-tail. In the second term denoting the Gaussian distribution, the N_G is the density of deep states, σ is the disorder spread, and E_{G0} is the mean energy of the deep traps.

We calculate a model DOS using eq 3 and then solve for the corresponding capacitance by integration with respect to ω according to eq 2. In doing so, the error between the measured and calculated capacitance is minimized, and the resulting fits are the black lines depicted in Figure 2a. Alternatively, we extract the DOS from capacitance−frequency measurements by computing the derivative $C/(\mathrm{d}\ln(\omega))$ in eq 2. Although there is considerable noise in the derivatives (Supporting

DOI: 10.1021/acsaelm.9b00009
ACS Appl. Electron. Mater. XXXX, XXX, XXX−XXX

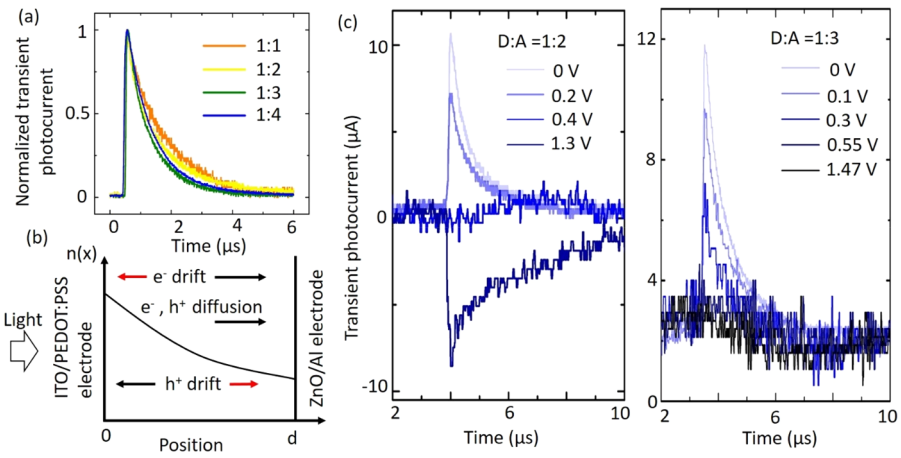

Figure 3. (a) Transient photocurrent at zero applied bias for devices with varying donor−acceptor ratios. (b) Schematics of drift and diffusion current directions. The black arrows are for drift at a bias voltage below the built-in voltage, while the red arrows are for above the built-in voltage. (c) Transient photocurrent under different applied bias for a photodiode with a D:A ratio of 1:2 or 1:3.

Information Figure S4), the obtained values match and confirm our DOS models.

The DOS for different D:A ratios are depicted in Figure 2b, and the best-fit values are listed in Table 1. For the D:A ratio of 1:4, 120 and 200 nm BHJ thicknesses show a similar DOS trend and therefore only 120 nm is listed in Table 1 as a representative. The uncertainty is low for the Gaussian distribution parameters describing the deep traps, as capacitance measurements are reliable for deep trap estimation corresponding to low frequencies. The high-frequency capacitance, however, can be affected by series resistance R when $\omega > 1/RC$. The recombination time limits the accuracy of capacitance measurements beyond 0.5 MHz. Thus, the accuracy decreases for DOS within 0.35 eV from the band edge, as calculated from eq 1 using the frequency limit. The parameters for exponential distribution in Table 1 are underestimates since carriers are not able to respond to fast ac perturbations, but values are probably correct within an order of magnitude.

There is a possibility that when changing the D:A ratio, the absorption of the CT state is affected as well.[31,32] In our BHJ, the CT state energy is estimated to be 1 eV (Supporting Information Figure S1), which corresponds to absorption at λ = 1240 nm. We do not observe a specific absorption hump around the CT state energy, probably because of the increasing nonradiative decay of CT excitons in our narrow bandgap system. In our devices, in lieu of direct CT state absorption, the sub-bandgap absorption is from band-tail states as illustrated in Supporting Information Figure S5. Light with energy lower than the polymer bandgap would generate excitons from these band-tail states located near the band edges, which migrate to the D−A interfaces to become CT state excitons.

The exponential DOS distribution characterizes the band-tail states located near the band edges. These band-tail states are shallow and provide states for photoexcited carriers to populate. Therefore, a wide band-tail distribution allows light absorption further into the sub-bandgap. The Gaussian DOS distribution characterizes the localized, deep trap states in the band gap. Carriers are trapped in these deep states that are very difficult to escape before recombination occurs, and hence deep traps contribute to poor charge transport, which is manifested as a decrease in EQE. From the Gaussian fits, devices with 1:3 and 1:4 ratios show fewer deep traps than the others, and this correlates to the EQE results. In summary, the Gaussian part of DOS contributes to the EQE loss and the exponential part of DOS contributes to sub-bandgap absorption. An illustration of the two DOS distributions is included in Supporting Information Figure S5.

In addition to the capacitance−frequency characteristics, the capacitance−voltage measurements in Figure 2c reveal two changes upon increasing the acceptor concentration in BHJs: (i) an increase in charge accumulation between 0 and 1 V and (ii) a rise in dielectric constant. The dielectric constant, ε, is calculated from the capacitance value at an applied bias of −4 V, where the device is fully depleted and the value is the geometric capacitance $C = \varepsilon\varepsilon_0 A/t$ with ε_0 being the vacuum permittivity. The ε increase agrees with prior work that reports higher polarizability[22] in BHJ blends than in their pristine constituents and increasing dielectric screening[21] with more fullerene. The enhanced dielectric constant presents an easily polarizable environment that reduces the Coulombic attraction between the electron and hole pair. As the exciton binding energy is lowered, photogeneration can become independent of the electric field,[33] because the dissociation process would not need an external bias to assist in separating electron−hole pairs. The devices here are not fully free of dissociation problems,[9,23] but the screening effect explains the characteristics in Figure 1b, which shows lower electric-field dependence as ε increases, when the D:A ratio is adjusted from 1:1 to 1:4.

Regarding the charge accumulation[34] between 0 and 1 V in Figure 2c, the capacitance reaches a maximum peak at an applied bias $V_{peakcap}$, at which point the applied electric field suppresses the built-in field, resulting in reduced charge extraction. The $V_{peakcap}$ is a measure of the potential barrier induced by charge accumulation. As the D:A ratio changes from 1:1 to 1:4, the $V_{peakcap}$ increases and indicates a higher potential barrier. The larger imbalance between donor and acceptor contents contributes to worse percolation transport for one carrier type (holes in this case) and leads to a rising barrier due to space charge accumulation. The effect of charge accumulation is also observable in the dark current−voltage characteristics in Supporting Information Figure S6, in which devices reach space-charge-limited conduction at smaller bias with higher acceptor concentration. The accumulated charge will alter the built-in electric field and potentially increase

DOI: 10.1021/acsaelm.9b00009
ACS Appl. Electron. Mater. XXXX, XXX, XXX−XXX

recombination. So far the analyses are for measurements in the dark; to further understand light response and recombination in organic SWIR photodiodes, transient photocurrent is measured to check for factors limiting the collection of photogenerated charge.

Transient Photocurrent Measurements. Measuring transient photocurrent allows us to probe the kinetics of dispersive transport and recombination. By using nanosecond laser pulses to photogenerate charge carriers, the transient photocurrent (TPC) shows the time it takes for carriers to be swept out before recombination. The photocurrent follows the stretched-exponential form[18] as shown in Figure 3a. After normalization to the peak amplitude, the TPC data indicate the device with the D:A ratio of 1:3 has the shortest transit time and the lowest recombination tail among all the blends. The TPC data before normalization are included in Supporting Information Figure S7.

In TPC measurements, the initial carrier concentration is depicted as in Figure 3b and is the same for both electrons and holes. Drift under an applied bias will produce current with the same sign because of the oppositely charged carriers. On the other hand, diffusive motion of the two carrier types will yield current with opposite directions and therefore opposite signs. When the applied bias increases from below to above the built-in voltage, the TPC is expected to change sign, because the internal electric-field direction is flipped. The built-in voltage of the devices is obtained from Figure 1b. In Figure 3c, the photodiode with 1:2 ratio switches its photocurrent sign as expected, as it transitions from zero to forward bias. In contrast, the device with 1:3 ratio does not show photocurrent for bias between 0.55 and 1.47 V. The forward-biased photocurrent is limited by recombination, since the electrons drifting toward the ITO electrode encounter accumulated holes and the carriers recombine and are not collected by the electrodes. It is also possible that as acceptor concentration increases, there is more hole trap density in the BHJ and the hole transport percolation pathways are disrupted. Thus, the increased charge accumulation with higher acceptor concentration leads to an extraction barrier.

The recombination in our devices is shown to be influenced by two factors, the potential barrier due to accumulated charge and the deep trap density. There is less accumulated space charge with decreasing acceptor concentration, but the reduced extraction barrier is offset by an increasing deep trap density. From DOS measurements, the device with 1:3 ratio has the lowest deep trap density and the highest EQE among the different blend compositions. The capacitance and transient photocurrent measurements are applicable to probe transport-recombination dynamics in the time scale of 0.1 μs or longer, and it would be relevant to study systems with ternary blends or polymer acceptors in the future.

For a photodetector, the signal-to-noise ratio, or detectivity, is $D^* = (A\Delta f)^{0.5}R/i_n$, where R is the responsivity, A is the effective photodetector area, Δf is the detection bandwidth, and i_n is the noise current. The current noise includes shot noise, thermal noise, and $1/f$ noise, and the total noise is the square root of the sum of squares of all components: $i_n = \sqrt{{i_{shot}}^2 + {i_{thermal}}^2 + {i_{1/f}}^2}$. A direct measurement of noise using a power spectral analyzer is essential to avoid an overestimation[9] of detectivity from using a shot−noise assumption of substituting $i_{shot} = \sqrt{2qI_{dark}\Delta f}$ as the i_n term. The measured noise spectral density in Figure 4a is not

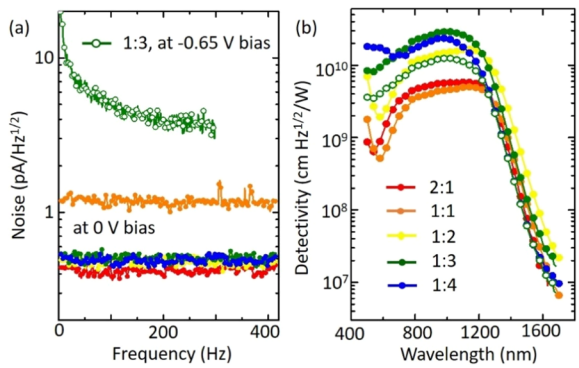

Figure 4. (a) Noise power spectral densities versus frequency. (b) Detectivities of the photodiodes versus incident wavelength, where the light source operates at 400 Hz. Solid symbols indicate devices at zero applied bias, and open symbols indicate a device at a reverse bias of −0.65 V.

significantly affected by the D:A ratio, and any difference is mainly due to processing variations. In our devices, the thermal noise can be calculated from the shunt resistance, R_{shunt}, by $i_{thermal} = \sqrt{4kT\Delta f/R_{shunt}}$, as shown in Supporting Information Figure S6. The calculated thermal noise values are listed in Supporting Information Table S1. The thermal noise comes close to the measured noise, indicating the thermal noise is the dominant noise source at zero bias for our SWIR devices here.

The detectivity is higher at 0 V than at reverse bias, since the device noise increases faster than the EQE at reverse bias.[35] In contrast, the noise level of typical visible photodiodes made of wide bandgap polymers is less sensitive to reverse bias, and therefore, strategically, their films can be thickened to suppress dark current and meanwhile high reverse bias is applied to compensate for EQE. This approach has not been effective for low-bandgap SWIR devices here due to increased recombination in thick films (performance of a device with 430 nm BHJ is included in Supporting Information Figure S6). The goal of selecting the BHJ thickness is to optimize the balance between the optical absorption and the charge transport efficiency. A film that is too thin has insufficient light absorption, while a thick film poses a long charge collection distance and reduces the internal electric field. Different systems have different optimized BHJ thicknesses, depending on the charge transport properties. In general, the optimized BHJ thickness for our material system is in the range of 150−200 nm.

The measured noise at reverse bias of −0.65 V in Figure 4a is an order of magnitude higher than at zero applied bias for the device with 1:3 D:A ratio, while the EQE improves only by 2× at reverse bias. Therefore, the resulting detectivity at reverse bias is lower than at zero bias, as seen in Figure 4b. The detectivities for different D:A ratios are calculated from the measured EQE and noise, and D^* reaches up to 3×10^{10} jones or cm $Hz^{1/2}$ W^{-1}.

Reconstructive Imaging in the SWIR Spectral Range Up to 1.3 μm. The organic photodiodes here show an extended spectral range beyond the visible spectrum and are used in single-pixel compressive imaging up to λ = 1.3 μm in the SWIR region. Unlike active-matrix pixel arrays,[4,5,23,36] a single-pixel camera configuration[37] simplifies detector requirements by leveraging computational techniques to process and reconstruct signals. A single photodetector works in conjunction with an array of spectral filters and a monochromatic light source as depicted in Figure 5a, and the detector captures

DOI: 10.1021/acsaelm.9b00009
ACS Appl. Electron. Mater. XXXX, XXX, XXX−XXX

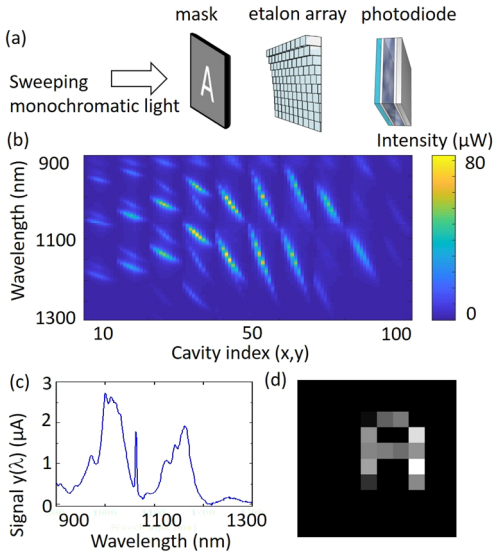

Figure 5. (a) Schematics of the measurement for image reconstruction. (b) Transmission characteristics of a 10 × 10 etalon array. (c) Photodiode current measured for a sample mask with the capital letter "A". The 1050 nm peak is due to the supercontinuum seed laser. (d) Reconstructed image using the data of parts b and c.

the signal $y(\lambda) = \int T(x,y,\lambda)\, \Phi(x,y)\, dx\, dy$. The spatial−spectral encoder is an etalon array[25] consisting of 10 × 10 cells, each made to vary in thickness to transmit a unique spectrum of light. In Figure 5b, the etalon array's spectral transmission pattern is measured to serve as the matrix $T(x,y,\lambda)$. This system can cover a wide spectral range from 500 to 1300 nm as seen in Supporting Information Figure S8. Image recovery is done with compressive sampling algorithms[37,38] using matrix calculations to minimize the error,[24] $|\sum(T\Phi) - y|^2$, between the measured signal, $y(\lambda)$, and the reconstructed image, $\Phi(x,y)$. For example, a projected image of the capital letter "A" is captured by the photodiode as the signal in Figure 5c. By using the etalon matrix values in the corresponding spectral range and computing through the compressive sensing algorithm, we are able to reconstruct an image successfully as shown in Figure 5d, which matches the projected pattern.

CONCLUSIONS

By examining the DOS through capacitance spectroscopy, increasing acceptor concentration decreases the deep trap density and raises the BHJ dielectric constant, both factors contributing to an enhancement in EQE. The EQE peaks at a 1:3 ratio and drops with further increase in acceptor, because of space charge accumulation and recombination issues as clarified by transient photocurrent measurements. Our SWIR photodiodes are easy to use with a compressive imaging system to image in the spectral range from visible wavelengths to 1.3 μm. The image reconstruction procedure is demonstrated to show promising potential for integrating organic SWIR devices in low-cost imaging systems.

ASSOCIATED CONTENT

Supporting Information

The Supporting Information is available free of charge on the ACS Publications website at DOI: 10.1021/acsaelm.9b00009.

Materials absorption, energy levels, measurement data fittings, and polymer synthesis procedures and the associated characterizations (PDF)

AUTHOR INFORMATION

Corresponding Author

*E-mail: tnn046@ucsd.edu

ORCID

Jason D. Azoulay: 0000-0003-0138-5961

Tse Nga Ng: 0000-0001-6967-559X

Notes

The authors declare no competing financial interest.

ACKNOWLEDGMENTS

Z.W., W.Y., and T.N.N. are grateful for the support from the National Science Foundation (Grant No. NSF ECCS-1839361). Part of the work was performed at the San Diego Nanotechnology Infrastructure of UCSD, which is supported by NSF ECCS-1542148. L.H., A.E.L., and J.D.A. are grateful for support from the National Science Foundation (Grant No. NSF OIA-1632825 and DGE-1449999) and the Air Force Office of Scientific Research (AFOSR) through the Organic Materials Chemistry Program (Grant No. FA9550-17-1-0261).

REFERENCES

(1) Wilson, R. H.; Nadeau, K. P.; Jaworski, F. B.; Tromberg, B. J.; Durkin, A. J. Review of Short-Wave Infrared Spectroscopy and Imaging Methods for Biological Tissue Characterization. *J. Biomed. Opt.* **2015**, *20* (3), 030901.

(2) Rauch, T.; Boberl, M.; Tedde, S. F.; Furst, J.; Kovalenko, M. V.; Hesser, G. G.; Lemmer, U.; Heiss, W.; Hayden, O. Near-Infrared Imaging with Quantum-Dot-Sensitized Organic Photodiodes. *Nat. Photonics* **2009**, *3* (6), 332−336.

(3) Baeg, K. J.; Binda, M.; Natali, D.; Caironi, M.; Noh, Y. Y. Organic Light Detectors: Photodiodes and Phototransistors. *Adv. Mater.* **2013**, *25* (31), 4267−4295.

(4) Pierre, A.; Arias, A. C. Solution-Processed Image Sensors on Flexible Substrates. *Flexible and Printed Electronics* **2016**, *1* (4), 043001.

(5) Jansen-van Vuuren, R. D.; Armin, A.; Pandey, A. K.; Burn, P. L.; Meredith, P. Organic Photodiodes: The Future of Full Color Detection and Image Sensing. *Adv. Mater.* **2016**, *28*, 4766−4802.

(6) Amit, M.; Mishra, R. K.; Hoang, Q.; Galan, A. M.; Wang, J.; Ng, T. N. Point-of-Use Robotic Sensors for Simultaneous Pressure Detection and Chemical Analysis. *Mater. Horiz.* **2019**, *6*, 604−611.

(7) Shen, L.; Lin, Y.; Bao, C.; Bai, Y.; Deng, Y.; Wang, M.; Li, T.; Lu, Y.; Gruverman, A.; Li, W.; et al. Integration of Perovskite and Polymer Photoactive Layers to Produce Ultrafast Response, Ultraviolet-to-near-Infrared, Sensitive Photodetectors. *Mater. Horiz.* **2017**, *4* (2), 242−248.

(8) Dou, L.; Liu, Y.; Hong, Z.; Li, G.; Yang, Y. Low-Bandgap Near-IR Conjugated Polymers/Molecules for Organic Electronics. *Chem. Rev.* **2015**, *115* (23), 12633−12665.

(9) Wu, Z.; Yao, W.; London, A. E.; Azoulay, J. D.; Ng, T. N. Elucidating the Detectivity Limits in Shortwave Infrared Organic Photodiodes. *Adv. Funct. Mater.* **2018**, *28* (18), 1800391.

(10) London, A.; Huang, L.; Zhang, B.; Oviedo, B.; Tropp, J.; Yao, W.; Wu, Z.; Wong, B.; Ng, T. N.; Azoulay, J. D. Donor−Acceptor Polymers with Tunable Infrared Photoresponse. *Polym. Chem.* **2017**, *8*, 2922−2930.

(11) Wu, Z.; Zhai, Y.; Kim, H.; Azoulay, J. D.; Ng, T. N. Emerging Design and Characterization Guidelines for Polymer-Based Infrared Photodetectors. *Acc. Chem. Res.* **2018**, *51* (12), 3144−3153.

(12) Hendriks, K. H.; Li, W.; Wienk, M. M.; Janssen, R. A. J. J. Small-Bandgap Semiconducting Polymers with High Near-Infrared Photoresponse. *J. Am. Chem. Soc.* **2014**, *136* (34), 12130−12136.
(13) Gong, X.; Tong, M.; Xia, Y.; Cai, W.; Moon, J. S.; Cao, Y.; Yu, G.; Shieh, C.-L. C.-L.; Nilsson, B.; Heeger, A. J. High-Detectivity Polymer Photodetectors with Spectral Response from 300 to 1450 nm. *Science* **2009**, *325* (5948), 1665−1667.
(14) Benduhn, J.; Tvingstedt, K.; Piersimoni, F.; Ullbrich, S.; Fan, Y.; Tropiano, M.; McGarry, K. A.; Zeika, O.; Riede, M. K.; Douglas, C. J.; et al. Intrinsic Non-radiative Voltage Losses in Fullerene-Based Organic Solar Cells. *Nat. Energy* **2017**, *2*, 17053.
(15) Street, R. A.; Krakaris, A.; Cowan, S. R. Recombination through Different Types of Localized States in Organic Solar Cells. *Adv. Funct. Mater.* **2012**, *22* (21), 4608−4619.
(16) Bisquert, J.; Bertoluzzi, L.; Mora-Sero, I.; Garcia-Belmonte, G. Theory of Impedance and Capacitance Spectroscopy of Solar Cells with Dielectric Relaxation, Drift-Diffusion Transport, and Recombination. *J. Phys. Chem. C* **2014**, *118* (33), 18983−18991.
(17) Street, R. A.; Yang, Y.; Thompson, B. C.; McCulloch, I. Capacitance Spectroscopy of Light Induced Trap States in Organic Solar Cells. *J. Phys. Chem. C* **2016**, *120* (39), 22169−22178.
(18) Street, R. A. Localized State Distribution and Its Effect on Recombination in Organic Solar Cells. *Phys. Rev. B: Condens. Matter Mater. Phys.* **2011**, *84* (7), 075208.
(19) Street, R. A. Electronic Structure and Properties of Organic Bulk-Heterojunction Interfaces. *Adv. Mater.* **2016**, *28* (20), 3814−3830.
(20) Mackenzie, R. C. I.; Shuttle, C. G.; Dibb, G. F.; Treat, N.; von Hauff, E.; Robb, M. J.; Hawker, C. J.; Chabinyc, M. L.; Nelson, J. Interpreting the Density of States Extracted from Organic Solar Cells Using Transient Photocurrent Measurements. *J. Phys. Chem. C* **2013**, *117*, 12407−12414.
(21) Bernardo, B.; Cheyns, D.; Verreet, B.; Schaller, R. D.; Rand, B. P.; Giebink, N. C. Delocalization and Dielectric Screening of Charge Transfer States in Organic Photovoltaic Cells. *Nat. Commun.* **2014**, *5*, 3245.
(22) Constantinou, I.; Yi, X.; Shewmon, N. T.; Klump, E. D.; Peng, C.; Garakyaraghi, S.; Lo, C. K.; Reynolds, J. R.; Castellano, F. N.; So, F. Effect of Polymer-Fullerene Interaction on the Dielectric Properties of the Blend. *Adv. Energy Mater.* **2017**, *7*, 1601947.
(23) Wu, Z.; Zhai, Y.; Yao, W.; Eedugurala, N.; Zhang, S.; Huang, L.; Gu, X.; Azoulay, J. D.; Ng, T. N. The Role of Dielectric Screening in Organic Shortwave Infrared Photodiodes for Spectroscopic Image Sensing. *Adv. Funct. Mater.* **2018**, *28* (50), 1805738.
(24) Kim, S.-J.; Koh, K.; Lustig, M.; Boyd, S.; Gorinevsky, D. An Interior-Point Method for Large-Scale L1-Regularized Least Squares. *IEEE Journal of Selected Topics in Signal Processing* **2007**, *1* (4), 606−617.
(25) Huang, E.; Ma, Q.; Liu, Z. Ultrafast Imaging Using Spectral Resonance Modulation. *Sci. Rep.* **2016**, *6*, 25240.
(26) Huang, E.; Ma, Q.; Liu, Z. Etalon Array Reconstructive Spectrometry. *Sci. Rep.* **2017**, *7*, 40693.
(27) Servaites, J. D.; Ratner, M. A.; Marks, T. J. Organic Solar Cells: A New Look at Traditional Models. *Energy Environ. Sci.* **2011**, *4* (11), 4410−4422.
(28) Lin, Y. L.; Fusella, M. A.; Rand, B. P. The Impact of Local Morphology on Organic Donor/Acceptor Charge Transfer States. *Adv. Energy Mater.* **2018**, *8*, 1702816.
(29) Walter, T.; Herberholz, R.; Müller, C.; Schock, H. W. Determination of Defect Distributions from Admittance Measurements and Application to $Cu(In,Ga)Se_2$ based Heterojunctions. *J. Appl. Phys.* **1996**, *80* (8), 4411−4420.
(30) Nicolai, H. T.; Mandoc, M. M.; Blom, P. W. M. Electron Traps in Semiconducting Polymers : Exponential versus Gaussian Trap Distribution. *Phys. Rev. B: Condens. Matter Mater. Phys.* **2011**, *83*, 195204.
(31) Vandewal, K.; Widmer, J.; Heumueller, T.; Brabec, C. J.; McGehee, M. D.; Leo, K.; Riede, M.; Salleo, A. Increased Open-Circuit Voltage of Organic Solar Cells by Reduced Donor-Acceptor Interface Area. *Adv. Mater.* **2014**, *26* (23), 3839−3843.
(32) Ullbrich, S.; Siegmund, B.; Mischok, A.; Hofacker, A.; Benduhn, J.; Spoltore, D.; Vandewal, K. Fast Organic Near-Infrared Photodetectors Based on Charge-Transfer Absorption. *J. Phys. Chem. Lett.* **2017**, *8* (22), 5621−5625.
(33) Street, R. A.; Cowan, S.; Heeger, A. J. Experimental Test for Geminate Recombination Applied to Organic Solar Cells. *Phys. Rev. B: Condens. Matter Mater. Phys.* **2010**, *82*, 12130.
(34) Zang, H.; Hsiao, Y.-C.; Hu, B. Surface-Charge Accumulation Effects on Open-Circuit Voltage in Organic Solar Cells Based on Photoinduced Impedance Analysis. *Phys. Chem. Chem. Phys.* **2014**, *16* (10), 4971−4976.
(35) Wu, Z.; Yao, W.; London, A. E.; Azoulay, J. D.; Ng, T. N. Temperature-Dependent Detectivity of Near-Infrared Organic Bulk Heterojunction Photodiodes. *ACS Appl. Mater. Interfaces* **2017**, *9*, 1654−1660.
(36) Ng, T. N.; Wong, W. S.; Chabinyc, M. L.; Sambandan, S.; Street, R. A. Flexible Image Sensor Array with Bulk Heterojunction Organic Photodiode. *Appl. Phys. Lett.* **2008**, *92* (21), 213303.
(37) Chan, W. L.; Charan, K.; Takhar, D.; Kelly, K. F.; Baraniuk, R. G.; Mittleman, D. M. A Single-Pixel Terahertz Imaging System Based on Compressed Sensing. *Appl. Phys. Lett.* **2008**, *93*, 121105.
(38) Duarte, M. F.; Davenport, M. A.; Takhar, D.; Laska, J. N.; Sun, T.; Kelly, K. F.; Baraniuk, R. G. Single-Pixel Imaging via Compressive Sampling. *IEEE Signal Processing Magazine* **2008**, *25* (2), 83−91.

DOI: 10.1021/acsaelm.9b00009
ACS Appl. Electron. Mater. XXXX, XXX, XXX−XXX